The Estimation of Free-Water Corrected Diffusion Tensors

Ofer Pasternak, Klaus Maier-Hein, Christian Baumgartner, Martha E. Shenton, Yogesh Rathi, and Carl-Fredrik Westin

Abstract Diffusion tensor imaging (DTI) is sensitive to micron scale displacement of water molecules, providing unique insight into microstructural tissue architecture. The tensors provide a compact way to describe the average of these displacements that occur within a voxel. However, current practical image resolution is in the millimeter scale, and thus diffusivities from many tissue compartments are averaged in each voxel, reducing the specificity of the measurement to subtle pathologies. In this chapter we review the free-water model, and use it to derive diffusion tensors following the elimination of the free-water component, that is assumed to originate from the extracellular space. Doing so, the resulting diffusion tensors and their derived indices measure the tissue itself, and are more sensitive to the geometry of the tissue, increasing the specificity to pathologies that affect brain tissue.

1 Introduction

Diffusion tensor imaging (DTI) along with other diffusion imaging analysis methods have became the leading MRI methodology to investigate the microstructure of brain tissue. In almost two decades of research since its inception [1], DTI studies

---

O. Pasternak (✉) • Y. Rathi • C.-F. Westin
Brigham and Women's Hospital, Harvard Medical School, Boston, MA, USA
e-mail: ofer@bwh.harvard.edu

K. Maier-Hein
German Cancer Research Center, Heidelberg, Germany

C. Baumgartner
King's College London, London, UK

M.E. Shenton
Brigham and Women's Hospital, Harvard Medical School, Boston, MA, USA

VA Boston Healthcare System, Brockton, MA, USA

were able to detect abnormalities that occur due to various brain disorders that include stroke, traumatic brain injuries, Multiple Sclerosis, Alzheimer's disease, Parkinson, Schizophrenia and many more disorders [2]. It appears that DTI indices are very sensitive to even subtle changes, either in the neuronal tissue or its surrounding, implicating a variety of pathologies, including demyelination, vasogenic and cytotoxic edema, inflammation, cell swelling, gliosis and other changes in the shape or sizes of neuron and glia cells [3]. Since DTI is very sensitive to many different pathologies, the challenge is to find methods that increase the specificity of the DTI indices, in such a way that allows better differentiation and diagnosis of the underlying processes that lead to the disorder, symptoms or pathology.

Diffusion MRI (dMRI) measures the displacement of water molecules, which in a typical brain imaging experiment displace a few tens of microns. This makes dMRI sensitive to normal and pathological architecture in the cellular scale. Nevertheless, current image resolution is in the millimeter scale, introducing partial volume of different tissue types – white matter, gray matter, glia cells, cerebrospinal fluid (CSF) – which reduces the sensitivity and specificity of most indices derived from dMRI and DTI [4]. Controlling for partial volume, and models that account for multiple compartments can therefore help in increasing the specificity, by determining in which of the compartments the abnormality occurs.

To date, most partial volume elimination methods concentrate on the case where two or more white matter fibers share a voxel (e.g., [5–7]). This chapter concentrates on the partial volume that occurs between the intra- and extra-cellular compartments. Correcting for extracellular water is required to eliminate CSF contamination, thus improving DTI's sensitivity in the vicinity of the ventricles [8] and important for the delineation of fibers that pass next to the CSF, such as the fornix [9, 10]. Moreover, the fractional volume of the extracellular water, relative to the remaining hindered or restricted water molecules, appears to provide important information with regard to pathological processes that modify the interstitial extracellular space, such as edema [9], neuroinflammation [11] and atrophy [12]. Indeed, the extracellular volume was shown to be sensitive to pathologies that appear in aging [12], schizophrenia [13], multiple-sclerosis [11], and Alzheimer's disease [14].

In this chapter we describe methods to estimate diffusion tensors that represent the signal following the elimination of free-water in the extracellular space. We start in Sect. 2 by describing the free-water model. We then show in Sect. 3 how to estimate the model parameters from a conventional, single-shell DTI acquisition, and from a more sophisticated multi-shell dMRI acquisition. In Sect. 4 we describe an alternative approach that estimates the model parameters in white matter while performing tractography. We conclude in Sect. 5 by demonstrating the effect of using free-water along with a clustering method to perform a group comparison between Alzheimer's disease patients and age matched controls.

2   The Free-Water Model

Free-water is defined as self-diffusing water molecules that do not experience restriction or hindrance from their surrounding. This definition depends on the amount of time in which the diffusion process is measured, as for infinitely long diffusion times, all water molecules will eventually hit an obstacle, whereas for infinitely short diffusion time, all water molecules are free to diffuse. In typical experimental setups the diffusion time is in the order of 30–50 ms which yields that in order for water molecules to diffuse freely they have to be a few tens of microns away from membranes and other cellular restrictions. The typical size of brain cells is usually lower than $10 \, \mu$m, and therefore in the brain, free-water can be found in the extra-cellular space. The diffusion coefficient of free-water is known, and depends on the temperature. For example, the diffusion coefficient of water in body temperature is $d_{water} = 3 \times 10^{-3}$ mm^2/s [15].

The free water model was first proposed by Pierpaoli and Jones [16]. The model estimates and corrects for the contribution of free-water [9]. The model assumes that the diffusion signal originates from two molecular compartments, co-existing within a voxel, with slow exchange between the compartments [9]:

$$\hat{A}_i(\mathbf{D}, f) = f \exp(-b_i \mathbf{g}_i^T \mathbf{D} \mathbf{g}_i) + (1 - f) \exp(-b_i d) . \qquad (1)$$

Here, $\hat{A}_i$ is the estimated signal (normalized by the b_0) of the i'th applied diffusion gradient with orientation $\mathbf{g}_i$, and b-value b_i. The first term reflects the tissue compartment, where $\mathbf{D}$ is the diffusion tensor of this compartment and f is the relative contribution of the compartment. The second term reflects an isotropic compartment, with a fixed diffusion coefficient, d, set to the diffusion coefficient of water in body temperature, 3×10^{-3} mm^2/s. Thus, the isotropic compartment models free-water, and is expected to measure molecules that are in the extra-cellular space, we call this compartment the free-water compartment. If the free-water compartment is eliminated, then the remaining compartment measures molecules that are close to tissue membranes, these are expected to include all the intracellular molecules, and some of the extracellular molecules that are not far enough from hindering obstacles such as cellular membranes.

When the free-water model was introduced it was different than other bi-compartmental models by the fact that the diffusion coefficient of the isotropic compartment was fixed. Prior to the free-water, other bi-compartment models either did not restrict the diffusivities of the compartments, resulting with "fast and slow" components (see for example [17]), or extremely restricted tissue compartment, with models such as the "ball-and-stick" [18] that separated all of the isotropic contribution (ball) from any remaining anisotropic contribution (stick). However, it was not clear how to relate the resulting compartments to biological compartments: In the fast-and-slow model, the fitting did not seem to match known values of intra- and extra-cellular volumes, leading to a debate on what are the sources of these

compartments [17]. With the "ball-and-stick" model, the orientation of the stick is generally aligned with that of white matter bundles, however the model does not allow assessment of other diffusion properties of the white matter, limiting the usability of this model to tractography studies. The fixed diffusivity of the free-water compartment, provides more of a biological compartmentalization to extra-cellular versus tissue compartments.

2.1 Free-Water Derived Maps

To acquire free-water maps, the free-water model in Eq. (1) has to be fitted with the measured dMRI signal. The outcome of this model-fit is a map of the tissue fraction (f) or a free-water map ($1 - f$). The free-water map, for example, has a range of [0–1] where values close to 0 are expected to be found in densely packed tissue, such as major fiber bundles, and values close to 1 are expected to be found in areas filled with CSF, such as the ventricles. In addition, the free-water eliminated tensor **D** can be further decomposed into scalar indices that can also be visualized as maps. These quantities include Fractional Anisotropy (FA), Mean diffusivity (MD), Axial and Radial diffusivity [19]. These tensor quantities describe properties of the tissue compartment, as such, the FA derived from the tissue compartment is called tissue-FA or FA_t. This notation differentiates the value from the FA that is derived from DTI, reflecting the anisotropy in the entire voxel (i.e., both the tissue and free-water compartments).

3 Fitting the Free-Water Model

The free-water model adds only one more parameter, f, to the DTI model. However, unlike DTI, the fitting of this bi-exponential model is highly unstable [17]. In order to stabilize the fit, we need to incorporate additional information that reduces the number of possible solutions.

3.1 Single Shell (DTI) Data

One way to stabilize a fit is by regularizing the fitted function. This is since requiring from a solution to be piece-wise smooth restricts considerably the solution space. Regularization is performed by including neighborhood information in the fitting of each voxel. This information requires that the solution not only fit the measurement, but will also be similar enough to the solution of the neighboring voxels. To stabilize the fitting process we use a regularization framework that adds

neighborhood constraints as additional information. We use a regularization method based on the Beltrami operator [20] by minimizing the following functional:

$$L(\mathbf{D}, f) = \int_\Omega \sum_{i \in G} ||\hat{A}_i - A_i|| + \alpha \sqrt{|\gamma(\mathbf{D})|} \,. \tag{2}$$

Here, Ω includes all voxels of interest, G are the indexes of all applied gradients and A_i are their signal normalized by the b_0. The parameter α scales the contribution of the Polyakov action regularization term (typically $\alpha = 1$ [9]), with $|\gamma(\mathbf{D})|$ as the determinant of the induced metric. Using the Einstein summation convention this metric has the form $\gamma_{\mu\nu}(\mathbf{p}) = \partial_\mu \mathbf{x}^m \partial_\nu \mathbf{x}^n h_{mn}(\mathbf{x})$, for each coordinate in the space: $\mathbf{p} = \{x, y, z\}$.

In order to define the spatial-feature metric $\mathbf{H} = \{h_{mn}\}$, one has to define the spatial, and the feature metrics. Selecting a Euclidean metric with the canonical tensor representation for the feature metric (distances between tensors), simplifies the analysis considerably, and is also preferred over other types of global tensor metrics [21]. As a result the vector $\mathbf{x}$ has the elements

$$\mathbf{x} = [D_{xx}, D_{yy}, D_{zz}, \sqrt{2}D_{xy}, \sqrt{2}D_{yz}, \sqrt{2}D_{xz}, x, y, z] \,.$$

The metric $\mathbf{H}$ for a Euclidean tensor space is simply a 9×9 diagonal matrix, with 1 for the last 3 diagonal entries (the spatial domain) and a constant for the remaining 6 diagonal entries. This leads to the motion equations for the six tensor elements, $\mathbf{x}^j$ with $j \in \{1, 2, \ldots, 6\}$:

$$\Delta \mathbf{x}^j = \sum_{i \in G} b_i (\hat{A}_i - A_i) \exp(-b_i \mathbf{g}_i^T \mathbf{D} \mathbf{g}_i) \left(\mathbf{g}_i^T \frac{\partial \mathbf{D}}{\partial \mathbf{x}^j} \mathbf{g}_i \right) + \frac{\alpha}{\sqrt{|\gamma|}} \partial_\mu \sqrt{|\gamma|} (\gamma^{\mu\nu} \partial_\nu \mathbf{x}^j) \,, \tag{3}$$

and for the fractional volume parameter:

$$\Delta f = \sum_{i \in G} -b_i (\hat{A}_i - A_i) \left(\exp(-b_i \mathbf{g}_i^T \mathbf{D}_t \mathbf{g}_i) - \exp(-b_i d) \right) \,. \tag{4}$$

The parameter f is maintained in the range $f \in [0, 1]$ by projecting values that exceed this range back within the range; see [9] for further constraints that can be enforced on this parameter. Importantly, due to the use of the Euclidean metric, and unlike the motion equations derived in [9], Eq. (3) does not have any Christoffel numbers, and therefore its calculation is simpler and faster. The second term in Eq. (3) is the Laplace-Beltrami operator, which is a piece-wise smooth, edge preserving tensor regularization operator [9, 20]. The final result is thus the parameters f and $\mathbf{D}$ that best fit the data while maintaining continuous tissue representation.
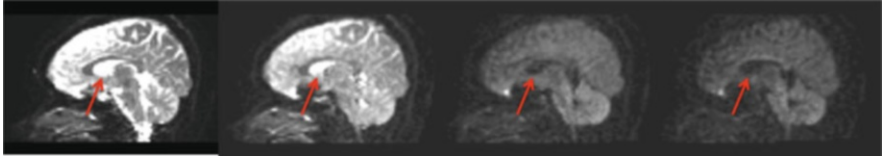
Fig. 1 Multi-shell acquisition. Diffusion signal for increasing b-values of (left to right) 0, 200, 900 and 1,400 mm^2/s in a mid-sagittal plane. The signal from free-water, such as in the ventricles (*red arrow*), decays into the noise floor faster than the signal of brain tissue

3.2 Multi-shell Free-Water Estimation

Regular DTI data is acquired using a single b-value, usually in the order of 1,000 s/mm^2, along with a non-diffusion-weighted image ($b = 0$ or b_0). The diffusion images are acquired using different gradient orientations, constituting a shell [22]. More elaborate acquisition schemes are available in which a number of different b-values are acquired, and a shell is acquired for each b-value, hence forming a multi-shell acquisition. Estimating the free-water fraction, f and the free-water eliminated tensor **D** using multi-shell data can be done using the same minimization defined in Eq. 2. However, when having multi-shell data, special properties of the multi-shell information can help initializing the estimation much closer to the minima [23]. When the initialization is good enough, the model fit may not require any further minimization.

The diffusivities of white and gray matter are considerably lower than those of free-water or CSF. Typically, in single shell DTI, healthy brain tissue has a quite homogeneous mean diffusivity of around 0.8 mm^2/s, 3–4 times slower than free-water. Therefore, the free-water signal is expected to decay faster than tissue, e.g., with a b-value of 900 s/mm^2 the tissue decays to 49 % of the signal while free-water decays to 7 % of the signal. Figure 1 shows an example of a multi-shell acquisition for a range of b-values. This range is achieved by modifying the diffusion gradient amplitude for fixed diffusion times. As expected, the free-water signal (mainly seen in the ventricles and around the parenchyma) attenuates faster than other brain tissue. The free-water signal diminishes completely into the noise floor for the higher b-values.

We calculate **D**$_H$, the apparent diffusion tensor for the high b-valued shells, as an estimator for **D** by minimizing:

$$\sum_{i \in G_H} ||\hat{b_0} \exp(-b_i \mathbf{g}_i^T \mathbf{D}_H \mathbf{g}_i) - E_i|| \, , \qquad (5)$$

where G_H are the indexes of all the applied gradients within the high b-valued shells, and E_i is the signal of the i'th acquired diffusion image, not normalized by the acquired b_0 (as opposed to its attenuation $A_i = E_i/E_0$). The acquired b_0 reflects the contribution of all spins within the voxel, including from free-water. Therefore,

the estimation of $\mathbf{D}_H$ requires the estimation of $\hat{b}_0$, which is the baseline image that would have been acquired in the case that the tensor $\mathbf{D}_H$ was the only component in the voxel. We minimize Eq. (5) using a linear least square (LLS) approach with $ln(\hat{b}_0)$ as one of the free parameters [8].

We estimate f, which reflects the extracellular relative volume in a voxel, using the low b-valued shells, which are in the range that still has signal from free-water. Given $\mathbf{D}_H$ as an estimate for $\mathbf{D}$, we can calculate f_L as an estimate for f using LLS by defining:

$$f_L = (\mathbf{a}^T \mathbf{a})^{-1} \mathbf{a}^T \mathbf{c} , \qquad (6)$$

where $\mathbf{c}_i = A_i - \exp(-b_i d)$ and $\mathbf{a}_i = \exp(-b_i \mathbf{g}_i^T \mathbf{D}_H \mathbf{g}_i) - \exp(-b_i d)$, and $i \in G_L$ being the indexes of the applied gradients in the low b-valued shells. Unlike our approach here, the single-shell free-water map estimation is initialized by the b_0 image alone, normalized by baseline values that assumed knowledge of voxels that have no tissue, and voxels that have no free-water [9]. This implicitly assumes that the T2 weighted images behave similarly across the entire brain, and that there are such baseline voxels. These assumptions are no longer required if using f_L and $\mathbf{D}_H$ as initialization.

3.3 Single- and Multi-shell Comparison

We test the multi-shell estimation on an acquisition optimized for the free-water estimation, having a single b $= 0$, $3 \times$ b $= 50$, $6 \times$ b $= 200$, $10 \times$ b $= 500$, $30 \times$ b $= 900$ and $16 \times$ b $= 1,400$, with gradient orientations designed as nested platonic solids, which means that each shell is rotationally invariant, and the shells complement each other to a rotationally invariant scheme [24]. Data was acquired on a 1.5 T scanner with 2.5 mm isotropic voxels and takes 9:20 min. We use the b $= 1,400$ and b $= 900$ shells to estimate $\mathbf{D}_H$, and the remaining shells to estimate f_L.

All data was motion and eddy-current corrected. We used 3D-Slicer's tensor estimation to calculate $\mathbf{D}_H$ by first omitting all images in G_L, including the b_0. We used Matlab (Natick, MA) to calculate f_L. The complete analysis for a whole brain takes less than 15 min on a 64-bit Linux machine with Xeon-E5530 processors, without taking advantage of multiple cores.

Both the multi-shell (Fig. 2a) and single-shell (using the b $= 900$ shell; Fig. 2b) estimations provide similar free-water maps, showing high values in the ventricles, and low values in the brain tissue, nicely depicting the extracellular volume. The color by orientation maps are similar as well. To better evaluate the differences between the maps, we plot free-water maps using a color-scale that increases the visibility of the lower values. We can then see that the multi-shell maps are not as smoothed as the single-shell maps, although both estimations used the same Laplace-Beltrami regularization operator. As a result the multi-shell map is

**Fig. 2 Optimized
multi-shell.** Multi-shell
regularized fitting
(**a**) provides a more detailed
extracellular volume (*left*)
and color by orientation
tissue tensor maps (*right*),
comparing with the
regularized single-shell fitting
(**b**). Small details are
preserved and there are less
artifacts (*white arrows*)
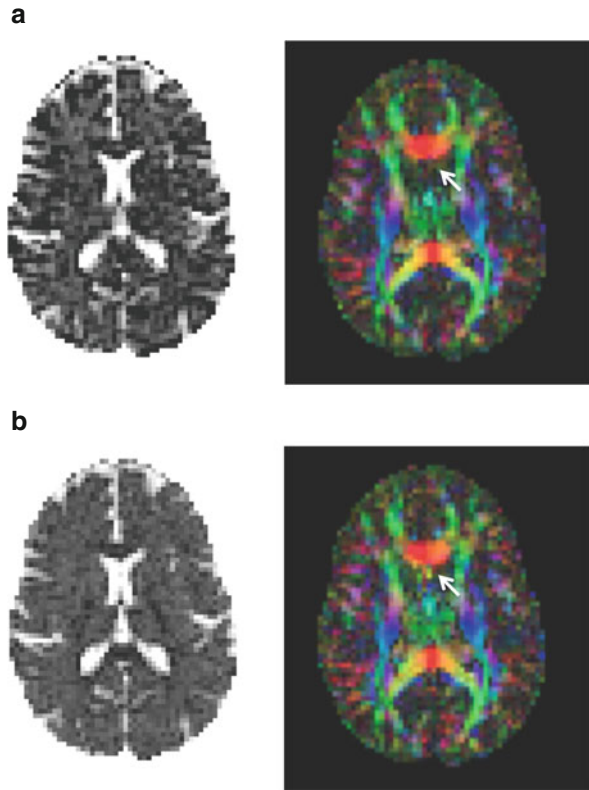
more detailed, allowing to better distinguish cortical structures. For this acquisition
scheme, the initialization, f_L is very similar to the final multi-shell free-water map.

4   Estimation via Filtered Tractography

An alternative to the gradient descent scheme proposed in the previous sections
is to perform filtered tractography [6] to estimate the free-water volume along
fiber tracts. The filtered tractography views tractography as a causal process and
incorporates information from neighboring voxels to aid in the model fit [25].
We arrive at each new position along the fiber based upon the model parameters
found at the previous position. As we examine the signal at each new position,
a Kalman filter recursively updates the underlying local model parameters based
on the last state, provides the variance of that estimate, and indicates the direction
in which to propagate tractography, where the estimation begins again. Recursive
estimation in this manner improves accuracy resolving individual orientations and
yields inherently smooth tracts despite the presence of noise and uncertainty.

4.1 State-Space Representation

To begin estimating within a finite dimensional state-space filter we need the method-specific definition of four filter components:

1. The system state $\mathbf{x}$: the model parameters
2. The state transition $\mathscr{F}[\cdot]$: how the model changes as we trace the fiber
3. The observation $v[\cdot]$: how the signal appears given a particular state
4. The measurement $\mathbf{y}$: the signal we are trying to fit the model to

Similar to the fitting of Eq. (2), the model parameters consist of the tensor of the tissue compartment, $\mathbf{D}$, and the fractional volume of the compartments, f. However, since the filtered tractography approach is restricted to following white matter, we can further simplify the model with the assumption that $\mathbf{D}$ is a cylindrical symmetric tensor, i.e., replace it with two eigenvalues, λ_1 and λ_2, and the principal direction $\mathbf{m}$. The system state is therefore:

$$\mathbf{x} = [\mathbf{m}, \lambda_1, \lambda_2, f]^T ,$$

Typically, the local fiber configuration does not undergo drastic change from one position to the next. For this reason we assume identity dynamics for the state transition function. The observation function is the reconstruction of the attenuated signal, given by the free-water model in Eq. (1), i.e.,

$$v[\mathbf{x}] = \hat{A}_1, \dots, \hat{A}_k ,$$

for k applied gradients. The measurement is the actual attenuated signal:

$$\mathbf{y} = A_1, \dots, A_k$$

interpolated directly from the diffusion weighted images at the current position.

4.2 Unscented Kalman Filter

Since the relation between the signal and the free-water model parameters are non-linear, we employ an unscented Kalman filter to perform the estimation [6]. Similar to a classical linear Kalman filtering, the unscented version seeks to reconcile the predicted state of the system with the measured signal. The filter process consists of two stages: first the system transition model is used to predict the next state and observation, then the new measurement is used to correct the state estimate.

The Kalman filter is a particle filter that for a solution space with a dimension n requires $2n + 1$ noisy realizations, in our case, $n = 6$. The Prediction begins with the formation of a set $\mathbf{X}_t = \{\chi_i\} \subset \mathbb{R}^n$ of $2n + 1$ sigma point states (or particles)

with associated convex weights, $w_i \in \mathbb{R}$. The sigma points are spread around the current state using a Gaussian distribution, with mean, $\mathbf{x}_t \in \mathbb{R}^n$, and covariance, $\mathbf{P}_t \in \mathbb{R}^{n \times n}$. The sigma points and their weights are defined as follows:

$$\chi_0 = \mathbf{x}_t$$

$$w_0 = \frac{\kappa}{(n + \kappa)} \quad w_i = w_{i+n} = \frac{1}{2(n + \kappa)} \tag{7}$$

$$\chi_i = \mathbf{x}_t + \left[\sqrt{(n + \kappa)\mathbf{P}_t} \right]_i \quad \chi_{i+n} = \mathbf{x}_t - \left[\sqrt{(n + \kappa)\mathbf{P}_t} \right]_i$$

where $[\cdot]_i$ denotes the i-th column of a matrix and κ is an adjustable scaling parameter. We used $\kappa = 0.01$ in all our experiments. Next, this set of sigma points is propagated through the state transition function, $\hat{\chi} = \mathscr{F}[\chi] \in \mathbb{R}^n$, to obtain a new predicted sigma point set: $\mathbf{X}_{t+1|t} = \{\mathscr{F}[\chi_i]\} = \{\hat{\chi}_i\}$. As mentioned above, we assume identity dynamics, i.e., $\mathbf{X}_{t+1|t} = \mathbf{X}_t$. The predicted system state is then calculated as the weighted average of the set,

$$\bar{\mathbf{x}}_{t+1|t} = \sum_i w_i \hat{\chi}_i , \tag{8}$$

The variability of the sigma points is calculated as:

$$\mathbf{P_{xx}} = \sum_i w_i (\hat{\chi}_i - \bar{\mathbf{x}}_{t+1|t})(\hat{\chi}_i - \bar{\mathbf{x}}_{t+1|t})^T + \mathbf{Q}, \tag{9}$$

where $\mathbf{Q}$ is the injected process noise bias used to ensure a non-null spread of sigma points and a positive-definite covariance. This procedure comprises the unscented transform used to estimate the behavior of a nonlinear function.

To obtain the predicted observation, we again apply the unscented transform, this time using the predicted states, $\mathbf{X}_{t+1|t}$, to estimate what we expect to observe from the hypothetical measurement of each state: $\varphi = v[\chi] \in \mathbb{R}^k$. This way we obtain the predicted set of observations, $\mathbf{Y}_{t+1|1} = \{v[\hat{\chi}_i]\} = \{\hat{\varphi}_i\}$, and may calculate its weighted mean and covariance,

$$\bar{\mathbf{y}}_{t+1|t} = \sum_i w_i \hat{\varphi}_i ,$$

$$\mathbf{P_{yy}} = \sum_i w_i (\hat{\varphi}_i - \bar{\mathbf{y}}_{t+1|t})(\hat{\varphi}_i - \bar{\mathbf{y}}_{t+1|t})^T + \mathbf{R}, \tag{10}$$

where $\mathbf{R}$ is the injected measurement noise bias again used to ensure a positive-definite covariance. The cross correlation between the estimated state and estimated measurement may also be calculated:

$$\mathbf{P_{xy}} = \sum_i w_i (\hat{\chi}_i - \bar{\mathbf{x}}_{t+1|t})(\hat{\varphi}_i - \bar{\mathbf{y}}_{t+1|t})^T . \tag{11}$$

Algorithm 1 Main loop repeated for each fiber

---

repeat
    Form the sigma points $\mathbf{X}_t$ around $\mathbf{x}_t$
    Predict the new sigma points $\mathbf{X}_{t+1|t}$ and observations $\mathbf{Y}_{t+1|t}$
    Compute weighted means, $\bar{\mathbf{x}}_{t+1|t}$, and $\bar{\mathbf{y}}_{t+1|t}$
    Compute covariances, $\mathbf{P_{xx}}, \mathbf{P_{xy}}, \mathbf{P_{yy}}$
    Update estimate $(\mathbf{x}_{t+1}, \mathbf{P}_{t+1})$ using scanner measurement $\mathbf{y}_{t+1}$
    Proceed in the estimated direction $\mathbf{m}_{t+1}$
until estimated model appears isotropic

As is done in the classic linear Kalman filter, the final step is to use the Kalman gain,

$$\mathbf{K} = \mathbf{P_{xx}}\mathbf{P_{yy}^{-1}}, \tag{12}$$

to correct our prediction and provide us with the final estimated system state, and with a covariance estimate to be used in the next steps:

$$\mathbf{x}_{t+1} = \bar{\mathbf{x}}_{t+1|t} + \mathbf{K}(\mathbf{y}_{t+1} - \bar{\mathbf{y}}_{t+1|t}) \tag{13}$$

$$\mathbf{P}_{t+1} = \mathbf{P_{xx}} - \mathbf{K}\mathbf{P_{yy}}\mathbf{K}^T. \tag{14}$$

To initialize this process we use $\mathbf{P}_0 = \mathbf{I}^{n \times n}$, and $\mathbf{x}_0$ is initialized by a single tensor estimation out of the acquired signal, y_0.

We continue in this manner until the model appears isotropic. Algorithm 1 outlines these steps.

4.3 Free-Water and Tensor Corrected Maps Following Filtered Tractography

The previous section outlines the estimation of the free-water model using filtered tractography, however, any model could be estimated using this approach (see in [26] for a number of different models that were included in the filtered tractography approach). We generated FA and FA_t maps based on a full brain tractography of a healthy volunteer. The maps were generated by recording the estimated model parameters for each voxel while performing the filtered tractography. Running the free-water model yielded free-water maps and FA_t maps. Running the filtered tractography on a model that does not include the fractional volume parameter yielded the DTI model and hence FA maps. Unlike the maps produced by the single- and multi-shell fit, these maps have values only in places where the tractography method identified fiber tracts. Therefore, the filtered tractography is limited to provide maps of white-matter alone.

Figure 3 compares axial slices of the FA and FA_t along with a difference map. Adding the free water term only adds small qualitative changes to the FA map. Looking at the difference maps (third from left) it can be seen that FA_t is overall

FA   FA$_t$ Difference (FA$_t$ – FA)   Free-Water
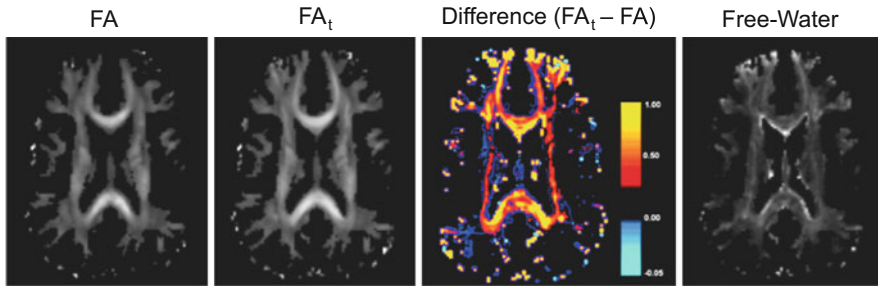
Fig. 3 Filtered tractography free-water maps. Maps of FA and FA$_t$ were generated while tracking white matter tracts in the entire brain. These maps are comparable to the single- and multi-shell maps, however, they have values only in white matter. The contrast of FA ranges between [0,1] and FA$_t$ is in general higher than FA especially in areas with significant partial volume, that have higher free-water values, as can be seen in the difference map and the free-water map

higher than FA. The biggest differences are observed around areas with partial volumes of CSF, around the ventricles and close the cortical areas. These areas match the ones with high free-water contents as can be seen from the free water map in the Fig. 3 (right). We observed, that including the free water term always increases the FA, decreases the Trace, and better fits the signal. The average free water content of all fibers was 19.09 %.

Next we compared the diffusion models on brain scans of 10 healthy human subjects. To generate the fiber tracts we began by seeding each voxel once, and traced the fibers for each of the diffusion models until the anisotropy threshold was reached, to arrive at a full brain tractography. From there we extracted the fibers that pass through the anterior limb of the internal capsule to filter out the respective tract under investigation. Fibers crossing the brain stem were excluded. We chose to perform full-brain tractography first in order to obtain more complete tract reconstructions. The fibers were expected to connect to the frontal gyri (green in Fig. 4). Furthermore, the fibers are expected not to be connected to the adjoining areas of precentral gyrus, and the caudal-middle-frontal gyrus (red in Fig. 4). The resulting tracts for all methods are shown in Fig. 4. Including free-water in the estimation produces a more complete fiber than without including free-water. However, the tracts did not reach all of the frontal gyri. When modifying the model to include three compartments, two with fiber tensors, and one with free-water, a much more complete delineation is achieved. This is suggesting that these fibers are affected by both partial volume with extra-cellular space, and crossing-fibers. The addition of the free-water to the two-tensor model produced slightly more complete fiber than without the free-water component, however, it also introduced a false-positive fiber that connected the cortico-spinal tracts with the caudal-middle-frontal gyrus.
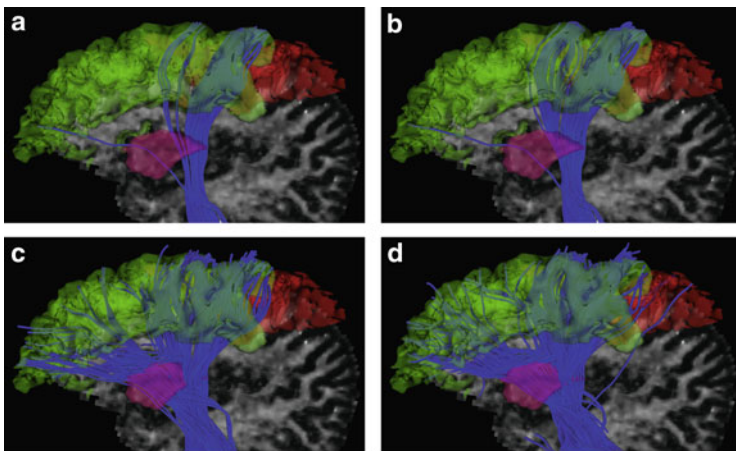
Fig. 4 Comparison of filtered tractography models. Fiber bundles passing through the anterior limb of the internal capsule (*purple*) to the target region (*green*), and the non-target region (*red*), as generated for four different filtered tractography models. Accounting for crossing-fibers by adding a second tensor component produces a much more complete fiber. Nevertheless, adding free-water provides an ever more complete representation of the fibers. (**a**) *DTI*. (**b**) *Free-water*. (**c**) *2-tensor*. (**d**) *2-tensor + free-water*

5 Free Water and Group Comparisons

Controlling for partial volume is especially important when comparing groups of subjects where changes in the volume might be part of the pathology. When performing group comparisons, it is usually advised to add the volume as a covariate, or to find analysis methods that obviate the volume changes all together [27]. One example for such an approach is tract based spatial statistics (TBSS) [28], which projects all the diffusivities onto a skeleton of the white-matter, thus representing the center of the fiber, which is supposed to be free of partial volume effects with the surrounding tissue. While this technique avoids regions of the fiber that are more prone to include partial volume effects and thus improves the accuracy of the statistics, at the same time many of the voxels are ignored, thus limiting the precision and statistical power of the analysis and potentially missing important information that might be in the data.

Alternatively, region-of-interest (ROI) analysis can manually achieve robust and accurate measurements that include as many voxels in the target region as possible. However, the ROI approach is prone to cause high inter- and intra-observer variability. In addition, in order to ensure accuracy and avoid the discussed biases due to partial volume, the regions have to be drawn in a very conservative fashion without the inclusion of surrounding structures or CSF. This again can lead to decreased precision and statistical power of the overall analysis.

In this section we demonstrate how free-water elimination can assist in controlling for partial volume in the delineation of ROIs. We apply a partial volume

clustering approach that combines a histogram based clustering analysis with an atlas-based placement of ROIs to avoid manual ROI placement and to circumvent the decreased sensitivity occurred when limiting the analysis to the white matter skeleton. The application of free-water enhances the partial volume clustering and provides the ability to differentiate macroscopic shrinking effects (i.e., atrophy) from microscopic alterations (such as cellular density changes). As a result we are able to compare microstructural changes that occur not only at the center but also at the periphery of fibers.

5.1 Partial Volume Clustering

Partial volume clustering is a technique for the robust extraction of diffusion indices from fiber bundles. It employs a probabilistic mixture model for differentiating fiber voxels from isotropic background, similarly to the procedure described in [29]. If a region includes both fiber and non fiber components, then using a probabilistic mixture model and histogram analysis, the ROI can be segmented into a fiber, a non fiber and a partial volume class on basis of a scalar anisotropy value that is derived on a voxel basis.

The classification algorithm assumes that the signal in a voxel is composed of signal from a fiber class (F), an isotropic background class (B), and a mixture class (M) [29]. The partial volume that the three classes occupy in the ROI is denoted by π_F, π_B and π_M respectively such that $\pi_F + \pi_B + \pi_M = 1$. The signal of the mixture class is given by

$$S_M = (1 - \rho)S_F + \rho S_B,$$

where ρ is the mixture parameter. The anisotropy index $a = 1 - (\lambda_2 + \lambda_3)/(2\lambda_1)$ [29, 30] is used as measure for the anisotropy, with λ_1, λ_2, and λ_3 being the sorted eigenvalues of the diffusion tensor. Let $P(a|F)$, $P(a|B)$ and $P(a|M)$ be the conditional probabilities that a is measured in fiber, background and mixture class. Then, the probability to measure a is

$$P(a) = \pi_F P(a|F) + \pi_B P(a|B) + \pi_M P(a|M) .$$

Here, $P(a|F)$ and $P(a|B)$ are modeled by Gaussian distributions with mean values m_F and m_B and variances σ_F and σ_B. By further assuming that ρ is uniformly distributed, $P(a|M)$ can be modelled [31] by

$$P(a|M) = \frac{1}{\sqrt{2\pi}} \int_0^1 \frac{d\rho}{\sqrt{\rho^2 \sigma_B^2 + (1-\rho)^2 \sigma_F^2}}$$
$$\cdot \exp\left(-\frac{((1-\rho)m_F + \rho m_B - a)^2}{2((1-\rho)^2 \sigma_F^2 + \rho^2 \sigma_B^2)}\right) \tag{15}$$

For the evaluation of a ROI, the free parameters $m_F, m_B, \sigma_F, \sigma_B, \pi_F, \pi_B$ and π_M must be determined. Thereto, the a-values of all voxels within the ROI are arranged in a histogram. Then, the free parameters are determined using a generalization of the EM algorithm [32] that was introduced by Laidlaw et al. [33]. Now, the conditional probabilities $P(a|F)$, $P(a|B)$ and $P(a|M)$ are known. Using Bayes' rule, we can find the class probabilities, for example for the fiber class,

$$P(F|a) = \pi_F P(a|F)/P(a) .$$

Then we can also calculate the expectation value for any arbitrary value V (e.g. for FA values) for a given class across a ROI, Ω. For example, the expectation value within the fiber class in a ROI of size n voxels is:

$$\langle V \rangle = \frac{1}{n\pi_F} \sum_{i \in \Omega} P(F|a_i)V_i$$

6 Partial Volume and Free-Water in the Corpus Callosum of Alzheimer's Disease

As a demonstration of the partial-volume clustering, we consider a problem of group comparison between a clinical population of Alzheimer's disease (AD) patients and normal controls. The disease manifests as a severe form of dementia and its signature pathologies are plaques and tangles. However, this neurodegenerative disease is also causing global alteration to the white-matter integrity via processes of inflammation and demyelination [34]. The Corpus-Callosum is known to be one of the prime white matter fibers to be affected in Alzheimer's [35]. To test the partial volume clustering we check if it is sensitive enough to identify the abnormalities on the Corpus-Callosum, and compare the results with the sensitivity of the TBSS approach.

6.1 Data Acquisition

A single shell (twice refocused) DTI data was collected on a 1.5 T (Symphony, Siemens) from 15 AD patients and 15 matched healthy controls. The data was collected using the following parameters: TR/TE 4,700/78 ms, FOV 240 mm, data matrix of 96×96 yielding an in-plane resolution of 2.5 mm, 50 axial slices with a thickness of 2.5 mm and no gap, with 6 gradient directions ($b = 1,000 \, \text{s/mm}^2$) and a b_0 image. This scheme was repeated 10 times. All images were corrected for motion and eddy currents (FSL, FLIRT), while compensating the gradient directions. Images were masked (FSL, BET) and the tensor toolkit was used for
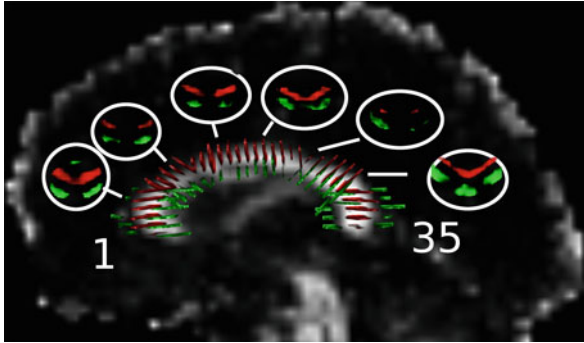
Fig. 5 Partial Volume Clustering. The Corpus Callosum was segmented into 35 ROIs along the mid-sagittal space. Partial volume clustering was run in each ROI, revealing that there was partial volume of the Corpus Callosum with its surrounding tissue. The "fiber" class is colored in *red*, "non-fiber" or background is *green* and "partial-volume" in *black*. Following clustering we use all of the "fiber" class to compare between subjects. Other methods, such as tract based spatial statistics (TBSS) use a subset of the "fiber" class (example, the skeleton) to conduct group comparisons. Including the entire "fiber" class in the analysis increases the number of samples and the statistical power (compare Fig. 6 for TBSS with Fig. 8 for the clustering approach)

tensor estimation (https://gforge.inria.fr/projects/ttk). Free-water corrected tensors and free-water maps were calculated using the single-shell estimation approach. From the tensors maps we extracted the radial diffusivity, $(\lambda_2 + \lambda_3)/2$, resulting with radial diffusivity maps and free-water corrected radial diffusivity maps that we used in order to compare between the groups.

6.2 Partial Volume Clustering Versus TBSS

Radial diffusivity is expected to be sensitive to pathological processes such as demyelination, that are common in AD, and we therefore compared the sensitivity of our partial-volume clustering approach to radial diffusivity abnormalities with the sensitivity of a TBSS approach.

For the clustering analysis, registration was performed in three steps directly on the tensor datasets using DTITK (http://www.nitrc.org/projects/dtitk):

1. A template was bootstrapped using the IXI aging template.
2. A population specific template space was created using affine and diffeomorphic registration.
3. Diffusion indices were extracted from the subjects by employing the probabilistic mixture model that was described in Sect. 5.1.

Thirty five fairly large ROIs were manually defined in template space using the open-source MITK Diffusion 2011 (www.mitk.org), and then placed along the Corpus Callosum using atlas based positioning, as illustrated in Fig. 5. The ROIs
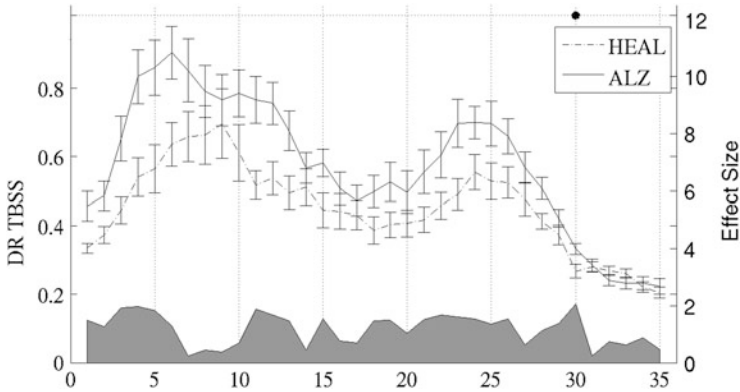
Fig. 6 Non-corrected radial diffusivities. Group differences of radial diffusivities (DR) between AD patients and normal controls based on TBSS analysis, show a single ROI that is significantly ($p < 0.05$) abnormal in AD (indicated with a *black circle*)

were defined in such a way that they parcellate the Corpus Callosum to even sections along the Corpus Callosum contour as it is found in the mid-sagittal slice. These ROIs included the Mid-Sagittal portion of the Corpus Callosum along with the tissue that surrounds it, thus each ROI included a partial volume of fiber, and non-fiber classes.

In addition to the partial volume clustering, the full TBSS pipeline was applied using the parameters suggested in [28]. The projection of the TBSS skeleton was applied to obtain radial diffusivities and free-water eliminated radial diffusivities skeletons. The Corpus-Callosum was identified in the mid-sagittal slice, and was linearly divided into 35 equal segments, to match the ROIs defined for the clustering approach.

We compared the two groups (AD and controls) separately for each ROI, using a two-sample unpaired t-test controlled for age with p = 0.05 as the threshold for significance.

6.3 Sensitivity to Abnormalities in Alzheimer's Disease

We first investigate abnormalities between the AD patients and the normal controls as they appear on the skeleton of the Corpus Callosum (using the TBSS analysis). We compare the sensitivity of the regular DTI radial diffusivity measure (Fig. 6), and compare it with the free-water corrected radial diffusivity (Fig. 7). We find that in general the radial diffusivity (either corrected or not corrected for free-water) in AD is higher than in controls. However, this difference was significant (indicated by black circles) in only one location when using non-corrected values, and in four locations when using corrected values. This is suggesting that in general the
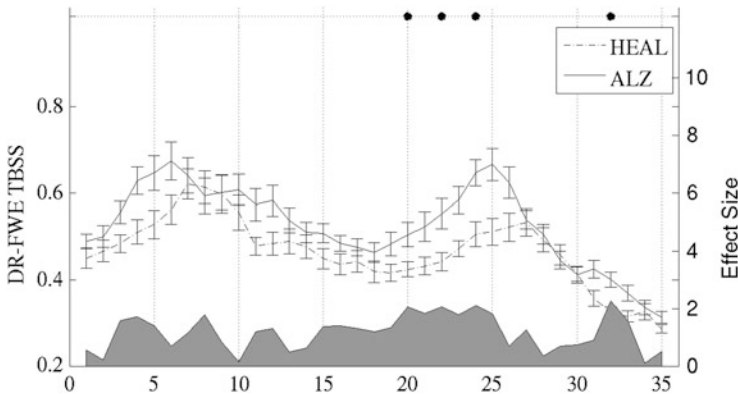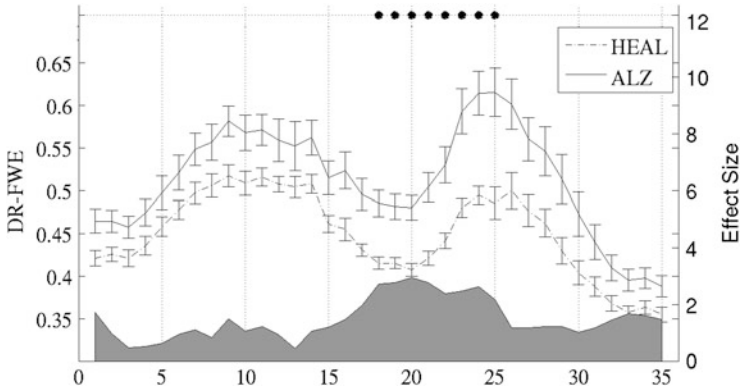
Fig. 7 Free-Water corrected radial diffusivities. Group differences of radial diffusivities corrected for free-water (DR-FWE) based on TBSS analysis reveal four ROIs with significant abnormalities. All the ROIs are in the posterior part of the Corpus-Callosum
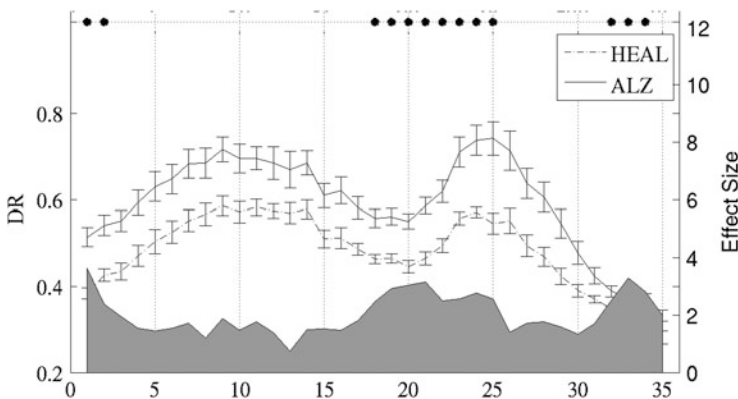
Fig. 8 Partial volume clustering of non-corrected radial diffusivity. Looking at the "fiber" class reveals many significant abnormalities ($p < 0.05$) forming two continuous clusters in the posterior part of the Corpus-Callosum. Looking on the "fiber" class reveals many more abnormalities than looking at the skeleton (see Fig. 6)

TBSS analysis is not extremely sensitive to the underlying pathology of AD, yet the sensitivity is increased when correcting for free-water. This is probably due to the fact that the corrected values are smoother than the non-corrected values.

We next compare the differences between AD patients and normal controls over the entire fiber cluster (as found by the partial volume clustering technique). We compare the non-corrected radial diffusivity values (Fig. 8) with the free-water corrected radial diffusivity values (Fig. 9). We find that the general trend of higher radial diffusivity in AD is preserved, however now there are many more ROIs in the Corpus-Callosum of AD that have a statistically significant increase. These ROIs are all located in the posterior region of the Corpus-Callosum (ROIs 18-25), suggesting

Fig. 9 Partial volume clustering of free-water corrected radial diffusivity. Consistent with the non-corrected findings (Fig. 6), many abnormalities form a cluster in the posterior part of the Corpus-Callosum, suggesting a demyelination related abnormality. The second cluster does not appear in the free-water analysis, suggesting that the underlying pathology there could be neuroinflammation or atrophy

that this part of the fiber has the most pathology. The increased sensitivity comparing to TBSS suggests that the pathology is mainly in the perimeters of the fiber, and not at its center, which is expected in cases of atrophy. Finally, the abnormal region can be divided to two parts, one that consistently shows abnormalities in both corrected and non-corrected values, and a second that is abnormal only in the non-corrected radial diffusivity values. This suggests the possibility of two different underlying pathology, demyelination, that increases radial diffusivity in both corrected and non-corrected values, versus inflammation, which is expected to increase radial diffusivity, but not corrected radial diffusivity.

7 Summary

Fitting the free-water model instead of the DTI model adds the extracellular volume as a new estimated biological parameter and provides tensor images that are more tissue specific [8–11]. This comes with a computational price, as the model is harder to estimate. The three approaches (single-shell, multi-shell, filtered tractography) discussed here provide means for estimation of the model parameters. This chapter covers the technical details involved in the estimation of the free-water maps and free-water corrected tensors, however, a systematic comparison is still in need, in order to better define when each method should be preferred.

It seems that the decision of which method to use should be driven by the type of data available, and the research question in mind. Specifically, if the research design can afford extra scan time, or if a multi-shell data is available, using the multi-shell estimation will be more stable and potentially more accurate then the single-shell

approach. With a multi-shell data we can relax assumptions and dependency on regularization that is required when fitting the model from a single-shell data. If the research question is specific to a certain white-matter bundle, then using the filtered tractography is a better selection. Of note, even though we presented filtered-tractography results on single-shell data, the method is straightforward to generalize for the multi-shell data.

Future work should also test the accuracy of the estimated parameters, through specially designed phantoms, or animal model scans. For example, the free-water estimation is biased by differences in T1 and T2 [9], it could be affected by temperature changes, and it would be interesting to see how it is affected by the types of noise that is expected in the dMRI acquisition. Another important task is to demonstrate pathological correlates of the free-water parameters. For example, it is clear that neuroinflammation and demyelination affects changes in the free-water and FA_t respectively, yet the specificity of these measures to the pathologies is not yet clear.

Since the introduction of the free-water model there were a number of higher order models that included a compartment of free-water with fixed diffusivities, along with various other compartments. For example, the The composite hindered and restricted water diffusion (CHARMED) model [36], the Axcaliber model [37], and more recently the neurite orientation dispersion and density imaging (NODDI) model [38]. Since it is easier to relate the free-water compartment to a biological compartment, the inclusion of this compartment in these models increase the specificity of the remaining compartments to the underlying tissue. These higher order methods typically require specialized acquisition, and it is yet to be determined whether the free-water compartment estimated in these measures matches the estimation of the free-water model as described here, although some preliminary results suggest that the values agree [39].

It is nevertheless clear that similar to the higher order models, the inclusion of the free-water parameter in the diffusion tensor model adds valuable new information to the study of the nervous system. We have demonstrated here the extra information that can be obtained in tractography, and in studying abnormalities related to AD, which is similarly applicable to many other brain disorders as well as for the study of normal development and aging.

References

1. Basser, P.J., Mattiello, J., LeBihan, D.: MR diffusion tensor spectroscopy and imaging. Biophys. J. **66**, 259–267 (1994)
2. Assaf, Y., Pasternak, O.: Diffusion tensor imaging (DTI)-based white matter mapping in brain research: a review. J. Mol. Neurosci. **34**(1), 51–61 (2008). doi:10.1007/s12031-007-0029-0

3. Alexander, A.L., Lee, J.E., Lazar, M., Field, A.S.: Diffusion Tensor Imaging of the Brain. Neurotherapeutics **4**(3), 316–329 (2007). doi:10.1016/j.nurt.2007.05.011
4. Vos, S.B., Jones, D.K., Viergever, M.A., Leemans, A.: Partial volume effect as a hidden covariate in DTI analyses. NeuroImage **55**(4), 1566–1576 (2011). doi:10.1016/j.neuroimage.2011.01.048
5. Pasternak, O., Assaf, Y., Intrator, N., Sochen, N.: Variational multiple-tensor fitting of fiber-ambiguous diffusion-weighted magnetic resonance imaging voxels. Magn. Reson. Imaging **26**(8), 1133–1144 (2008)
6. Malcolm, J.G., Shenton, M.E., Rathi, Y.: Filtered multi-tensor tractography. IEEE Trans. Med. Imaging **29**, 1664–1675 (2010). doi:10.1109/TMI.2010.2048121
7. Alexander, D.: Multiple-fibre reconstruction algorithms for diffusion MRI. Ann. N. Y. Acad. Sci. **1046**, 113–133 (2005)
8. Jones, D.K., Cercignani, M.: Twenty-five pitfalls in the analysis of diffusion MRI data. NMR Biomed. **23**(7), 803–820 (2010). doi:10.1002/nbm.1543
9. Pasternak, O., Sochen, N., Gur, Y., Intrator, N., Assaf, Y.: Free water elimination and mapping from diffusion mri. Magn. Reson. Med. **62**(3), 717–730 (2009)
10. Metzler-Baddeley, C., O'Sullivan, M.J., Bells, S., Pasternak, O., Jones, D.K.: How and how not to correct for CSF-contamination in diffusion MRI. NeuroImage **59**(2), 1394–1403 (2012). doi:10.1016/j.neuroimage.2011.08.043
11. Wang, Y., Wang, Q., Haldar, J.P., Yeh, F.C., Xie, M., Sun, P., Tu, T.W., Trinkaus, K., Klein, R.S., Cross, A.H., Song, S.K.: Quantification of increased cellularity during inflammatory demyelination. Brain **134**(12), 3590–3601 (2011). doi:10.1093/brain/awr307
12. Metzler-Baddeley, C., Jones, D., Belaroussi, B., Aggleton, J., O'Sullivan, M.: Frontotemporal connections in episodic memory and aging: A diffusion MRI tractography study. J. Neurosci. **31**(37), 13236–13245 (2011)
13. Pasternak, O., Westin, C.F., Bouix, S., Seidman, L.J., Goldstein, J.M., Woo, T.U.W., Petryshen, T.L., Mesholam-Gately, R.I., McCarley, R.W., Kikinis, R., et al.: Excessive extracellular volume reveals a neurodegenerative pattern in schizophrenia onset. J. Neurosci. **32**(48), 17365–17372 (2012)
14. Fritzsche, K., Stieltjes, B., van Bruggen, T., Meinzer, H.P., Westin, C.F., Pasternak, O.: A combined approach for the elimination of partial volume effects in diffusion MRI. In: Proceedings of the 20th ISMRM, Melbourne, p. 3548 (2012)
15. Harris, K.R., Woolf, L.A.: Pressure and temperature dependence of the self diffusion coefficient of water and oxygen-18 water. J. Chem. Soc. Faraday Trans. 1 **76**, 377–385 (1980). doi:10.1039/F19807600377, http://dx.doi.org/10.1039/F19807600377
16. Pierpaoli, C., Jones, D.: Removing CSF contamination in brain DT-MRIs by using a two-compartment tensor model. In: Proceedings of the 12th ISMRM, Kyoto, p. 1215 (2004)
17. Mulkern, R.V., Haker, S.J., Maier, S.E.: On high b diffusion imaging in the human brain: ruminations and experimental insights. Magn. Reson. Imaging **27**(8), 1151–1162 (2009). doi:10.1016/j.mri.2009.05.003
18. Behrens, T.E., Woolrich, M.W., Jenkinson, M., Johansen-Berg, H., Nunes, R.G., Clare, S., Matthews, P.M., Brady, J.M., Smith, S.M.: Characterization and propagation of uncertainty in diffusion-weighted MR imaging. Magn. Reson. Med. **50**(5), 1077–1088 (2003)
19. Pierpaoli, C., Jezzard, P., Basser, P., Barnett, A., Di Chiro, G.: Diffusion tensor MR imaging of the human brain. Radiology **201**(3), 637–648 (1996)
20. Gur, Y., Pasternak, O., Sochen, N.: Fast GL(n)-invariant framework for tensors regularization. Int. J. Comput. Vis. **85**(3), 211–222 (2009)
21. Pasternak, O., Sochen, N., Basser, P.J.: The effect of metric selection on the analysis of diffusion tensor MRI data. NeuroImage **49**(3), 2190–2204 (2010). doi:10.1016/j.neuroimage.2009.10.071, http://dx.doi.org/10.1016/j.neuroimage.2009.10.071
22. Jones, D.K.: The effect of gradient sampling schemes on measures derived from diffusion tensor MRI: a monte carlo study. Magn. Reson. Med. **51**(4), 807–815 (2004)

23. Pasternak, O., Shenton, M., Westin, C.F.: Estimation of extracellular volume from regularized multi-shell diffusion MRI. In: Proceedings of the MICCAI, Nice, pp. 305–312 (2012)
24. Westin, C.F., Pasternak, O., Knutsson, H.: Rotationally invariant gradient schemes for diffusion MRI. In: Proceedings of the 20th ISMRM, Melbourne (2012)
25. King, M.D., Gadian, D.G., Clark, C.A.: A random effects modelling approach to the crossing-fibre problem in tractography. NeuroImage **44**, 753–768 (2009)
26. Baumgartner, C., Michailovich, O., Levitt, J., Pasternak, O., Bouix, S., Westin, C., Rathi, Y.: A unified tractography framework for comparing diffusion models on clinical scans. In: Computational Diffusion MRI Workshop of MICCAI, Nice, pp. 27–32 (2012)
27. Metzler-Baddeley, C., O'Sullivan, M.J., Bells, S., Pasternak, O., Jones, D.K.: How and how not to correct for CSF-contamination in diffusion MRI. NeuroImage **59**(2), 1394–1403 (2012). doi:10.1016/j.neuroimage.2011.08.043
28. Smith, S.M., Jenkinson, M., Johansen-Berg, H., Rueckert, D., Nichols, T.E., Mackay, C.E., Watkins, K.E., Ciccarelli, O., Cader, M.Z., Matthews, P.M., Behrens, T.E.J.: Tract-based spatial statistics: voxelwise analysis of multi-subject diffusion data. NeuroImage **31**(4), 1487–1505 (2006). doi:10.1016/j.neuroimage.2006.02.024, http://dx.doi.org/10.1016/j.neuroimage.2006.02.024
29. Schlueter, M., Stieltjes, B., Hahn, H.K., Rexilius, J., Konrad-verse, O., Peitgen, H.O.: Detection of tumour infiltration in axonal fibre bundles using diffusion tensor imaging. Int. J. Med. Robot. **1**(3), 80–86 (2005). doi:10.1002/rcs.31, http://dx.doi.org/10.1002/rcs.31
30. Stieltjes, B., Schlüter, M., Didinger, B., Weber, M.A., Hahn, H.K., Parzer, P., Rexilius, J., Konrad-Verse, O., Peitgen, H.O., Essig, M.: Diffusion tensor imaging in primary brain tumors: reproducible quantitative analysis of corpus callosum infiltration and contralateral involvement using a probabilistic mixture model. NeuroImage **31**(2), 531–542 (2006). doi:10.1016/j.neuroimage.2005.12.052, http://dx.doi.org/10.1016/j.neuroimage.2005.12.052
31. Noe, A., Gee, J.C.: Partial volume segmentation of cerebral mri scans with mixture model clustering. In: IPMI, Davis, pp. 423–430 (2001)
32. McLachlan, G.J., Krishnan, T.: The EM Algorithm and Extensions. Wiley Series in Probability and Statistics (2007). doi:10.1002/9780470191613
33. Laidlaw, D.H., Fleischer, K.W., Barr, A.H.: Partial-volume bayesian classification of material mixtures in MR volume data using voxel histograms. IEEE Trans. Med. Imaging **17**(1), 74–86 (1998). doi:10.1109/42.668696, http://dx.doi.org/10.1109/42.668696
34. Weiner, H.L., Selkoe, D.J.: Inflammation and therapeutic vaccination in CNS diseases. Nature **420**(6917), 879–884 (2002). doi:10.1038/nature01325, http://www.nature.com/nature/journal/v420/n6917/full/nature01325.html
35. Agosta, F., Pievani, M., Sala, S., Geroldi, C., Galluzzi, S., Frisoni, G.B., Filippi, M.: White matter damage in alzheimer disease and its relationship to gray matter atrophy. Radiology **258**(3), 853–863 (2011). doi:10.1148/radiol.10101284, http://radiology.rsna.org/content/258/3/853.long
36. Assaf, Y., Basser, P.J.: Composite hindered and restricted model of diffusion (CHARMED) MR imaging of the human brain. NeuroImage **27**(1), 48–58 (2005). doi:10.1016/j.neuroimage.2005.03.042, http://www.sciencedirect.com/science/article/pii/S1053811905002259
37. Assaf, Y., Blumenfeld-Katzir, T., Yovel, Y., Basser, P.J.: Axcaliber: a method for measuring axon diameter distribution from diffusion MRI. Magn. Reson. Med. **59**(6), 1347–1354 (2008)
38. Zhang, H., Schneider, T., Wheeler-Kingshott, C.A.M., Alexander, D.C.: NODDI: Practical in vivo neurite orientation dispersion and density imaging of the human brain. NeuroImage **61**(4), 1000–1016 (2012)
39. van Bruggen, T., Zhang, H., Pasternak, O., Meinzer, H.P., Stieltjes, B., Fritzsche, K.H.: Free-water elimination for assessing microstructural gray matter pathology - with application to alzheimer's disease. In: Proceedings of the 21th ISMRM, Salt Lake City, p. 790 (2013)